

# Strong pinning in thick $\text{YBa}_2\text{Cu}_3\text{O}_7$ layers mediated by catalysis of a new long-period metastable cuprate phase

Vyacheslav F. Solovyov,<sup>1,a)</sup> Katherine Develos-Bagarinao,<sup>2</sup> Qiang Li,<sup>1</sup> Wei-Dong Si,<sup>1</sup> Li-Jun Wu,<sup>1</sup> Juan Zhou,<sup>1</sup> Harold Wiesmann,<sup>1</sup> and Jie Qing<sup>1</sup>

<sup>1</sup>*Department of Condensed Matter Physics and Materials Science, Brookhaven National Laboratory, Upton, New York 11973, USA*

<sup>2</sup>*National Institute of Advanced Industrial Science and Technology, AIST Tsukuba Central 2, 1-1-1 Umezono Tsukuba, Ibaraki 305-8568, Japan*

(Received 4 September 2010; accepted 21 October 2010; published online 8 December 2010)

Catalysts are widely utilized to promote reactions in liquid and gaseous phases but are rarely encountered in solid state synthesis. Here we use catalytically active (001) ceria buffers to modify the structure of the epitaxial high temperature superconductor  $\text{YBa}_2\text{Cu}_3\text{O}_7$ . The modification is achieved by catalytically-assisted synthesis of a previously unknown metastable phase. The new phase, a long-period (3.5 nm) perovskite, intercalates into the  $\text{YBa}_2\text{Cu}_3\text{O}_7$  matrix without negatively affecting the critical temperature of the film. Analysis of electron microscopy and synchrotron x-ray diffraction data allow identification of the phase as a long-period  $\text{YBa}_2\text{Cu}_3\text{O}_7$  derivative formed through short-range cation displacement. The 0.8  $\mu\text{m}$  thick films exhibit strong enhancement of the critical current density, reaching a maximum of 4.2 MA/cm<sup>2</sup> at 77 K. The result emphasizes the critical role of catalysis for synthesis of novel complex materials. © 2010 American Institute of Physics. [doi:10.1063/1.3517467]

## I. INTRODUCTION

Strongly correlated materials often undergo nanoscale phase transitions resulting in the emergence of new phenomena.<sup>1</sup> High temperature superconductors (HTSs) exhibit multiple nanoscale ordering patterns, involving vacancy,<sup>2,3</sup> cation,<sup>4</sup> and magnetic ordering. Soon after the discovery of HTS, Zandbergen *et al.*<sup>4</sup> observed that the layered structure of  $\text{YBa}_2\text{Cu}_3\text{O}_7$  (YBCO) makes this superconductor susceptible to a specific type of cation ordering, namely, the insertion of extra copper oxide (CuO) planes. The tendency of YBCO to incorporate CuO layers turned out to be of limited practical use, since extended CuO planes provide strong pinning only when the Abrikosov vortices are almost parallel to the film surface.<sup>5</sup> This is a major reason why the development of YBCO-based superconducting wire<sup>6,7</sup> has concentrated on the design of artificial pinning centers<sup>8,9</sup> rather than on utilizing structural chemistry of cuprates. This technology may be reaching its limit, since the  $J_c$  typically reaches a maximum at several percent mole fraction of foreign precipitates [e.g., 5% mole fraction for  $\text{BaZrO}_3$  (Ref. 10) and  $\text{Y}_2\text{O}_3 + \text{BaZrO}_3$  (Ref. 11)], partially because in some cases the high density of defects reduces the critical temperature<sup>10</sup> of the YBCO matrix, negating the advantage of stronger pinning. Additionally many effective pinning centers, such as  $\text{BaZrO}_3$  nanorods, can only be formed at a relatively low YBCO growth rate,<sup>8,10</sup> which may be a practical limitation for large-scale production.

The methods currently used to grow films of complex oxides can be described as adaptations of traditional thin film epitaxy. The substrate serves as a template to transfer the desired crystallographic orientation to the epitaxial layer of a

well-known bulk material, YBCO. In this work we broaden this concept and use the substrate as a catalyst for the synthesis of new metastable materials. A metastable material does not exist in the bulk, because under any growth conditions its critical nucleus is unstable either due to unfavorable thermodynamics or competition from dominant phases. A metastable phase can emerge under two conditions: (i) the substrate is active enough, i.e., it provides nucleation sites with low enough surface energy to make the critical nucleus stable; (ii) the growth conditions are set to suppress the formation of dominant bulk phases, which otherwise would occupy the nucleation sites. Here we show, that if these two conditions are met, new metastable phases do emerge. Remarkably, the presence of one of the phases, a long period YBCO derivative, dramatically improves the superconducting properties of YBCO films.

## II. EXPERIMENT

To assist the formation of the epitaxial phases, we use 15 nm thick (001) ceria buffers deposited on single crystal substrates. Ceria is a well known catalytically-active material<sup>12</sup> widely used as a template for YBCO epitaxy.<sup>13,7</sup> The ceria buffers were deposited on (001) yttria-stabilized zirconia (YSZ) and r-cut sapphire substrates by pulsed laser deposition at a substrate temperature 650 °C ((001) YSZ, CeO-20 sample) and 700 °C (r-cut sapphire, CeO-100) sample. The substrates were annealed at 1000 °C in flowing oxygen to adjust the lateral grain size. The lateral grain size is the critical buffer characteristic because the activity of (001) ceria buffer for YBCO epitaxy depends on the ceria buffer grain size and lateral inhomogeneous strain level.<sup>14,15</sup> Small-grain (<20 nm lateral grain size) strained buffers develop a dense array of nucleation sites generated by threading dislocation

<sup>a)</sup>Electronic mail: solov@bnl.gov.

outcrops. A buffer with a 20 nm lateral grain size delivers approximately fivefold higher density of YBCO nuclei than a buffer with  $>100$  nm grains under identical processing conditions. The penalty associated with the use of small-grain buffers is a relatively high mosaic spread,  $\sim 1^\circ$ , of the epitaxial YBCO layer, compared to  $<0.1^\circ$  when a single crystal wafer is used.<sup>14</sup> However, this is a minor disadvantage considering that the transport superconducting properties are only weakly sensitive to the grain mis-orientations up to  $4^\circ$ .<sup>16,17</sup>

The fluorinated metal-organic deposition (MOD) precursor layers were deposited by American Superconductor Corporation by spin-coating precursors identical to those used in the production of the second-generation superconducting wire.<sup>18</sup> The precursor film had the cation composition of Y:Dy:Ba:Cu=1:0.5:2:3; Dysprosium metal was added to enhance pinning at high fields, at the same time Dy addition suppressed formation of Y248-type stacking faults (SFs).<sup>5</sup> The films were converted to (001) YBCO by heat-treatment at 780 °C in atmosphere comprised of 22 Torr of water vapor and 40–200 mTorr of oxygen, as previously described.<sup>14</sup> The YBCO growth rate was set at 0.6 nm/s by placing the sample in an annealing cell. In the course of these experiments, six film samples were prepared for each of the two kinds of substrate.

After the conversion, the samples were annealed in flowing oxygen at 400 °C for 30 min. The samples were also subjected to additional annealing at higher temperatures. After each treatment the samples were held 30 min at 400 °C to restore the oxygen stoichiometry. The critical current density and the critical temperature were then measured by the magnetization method using Quantum Design superconducting quantum interference device (SQUID) magnetometer. Bean model has been used to calculate the critical current density and the irreversibility field.

The x-ray diffraction (XRD) experiment was carried out at the X-18A beamline of the National Synchrotron Light Source. X-18A is a bending magnet beamline designed for high-flux single-crystal diffraction. Transmission electron microscopy (TEM) characterization was performed using a JEOL 2100 electron microscope. The TEM samples were prepared by mechanical polishing and subsequent focused ion beam milling.

### III. RESULTS

#### A. Synthesis and properties of long-period YBCO derivatives

The advantage of strong substrate catalysis is demonstrated by comparing the performance of 0.8  $\mu\text{m}$  YBCO layers deposited on two types of ceria buffers (Fig. 1): CeO-100 is a film deposited on a buffer with large (100 nm average lateral diameter) grains with atomically flat (001) terminations and low activity, while CeO-20 is a typical example of a film deposited on small-grain (20 nm lateral grain size), strained buffer with high activity. The YBCO films were grown by a MOD process from fluorinated precursors as described in the Methods section. Figure 1(a) compares the in-field critical current densities of the CeO-100 and CeO-20

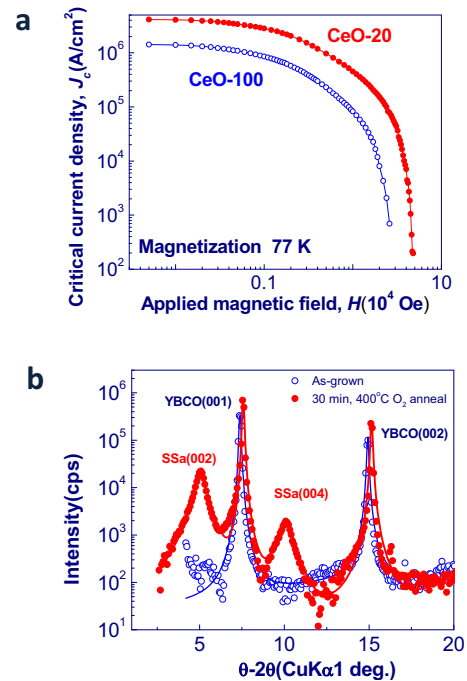


FIG. 1. (Color online) Enhancement of the critical current density of a 0.8  $\mu\text{m}$  film due to high activity of small-grain CeO-20 substrate at 77 K. (a) Open symbols correspond to the film grown on the large grain ceria buffer, CeO-100, while closed symbols represent film on a small-grain buffer, CeO-20. The oxygen partial pressure values, optimized for each sample, are 100 mTorr for the CeO-100 sample and 65 mTorr for the CeO-20 sample. The measurements were performed at 77 K, the external magnetic field,  $H$  is normal to the film  $c$ -axis ( $H \parallel c$ ). (b) Development of a long-period phase after oxygen annealing at 400 °C (closed symbols) of as-grown CeO-20 film sample (open symbols). The diffraction spectrum of the annealed sample (closed symbols) shows two additional superstructure peaks, labeled SSa(002) and SSa(004), corresponding to  $d$ -spacing of 1.748(1) nm and 0.879(2) nm, respectively. The formation of the new phase is related to the high performance of CeO-20 samples. The solid lines are Pearson7 approximations used in the line profile analysis. The spectrum was acquired using 10 kV synchrotron radiation with  $2\theta$  values converted to their  $\text{Cu } K_{\alpha 1}$  equivalent.

0.8  $\mu\text{m}$  samples at 77 K,  $H \parallel c$ -axis orientation. Both samples were processed at conditions optimized for maximum critical current density,  $J_c$ , value. Sample CeO-100 represents a typical behavior of a 0.8  $\mu\text{m}$  thick film deposited on a single-crystal substrate or a large grain buffer.<sup>19</sup> The  $J_c$  of a CeO-100 sample reaches a maximum of  $\sim 2$  MA/cm<sup>2</sup> at  $p(\text{O}_2) = 100$  mTorr and starts to fall rapidly at lower  $p(\text{O}_2)$  due to the de-coupling of YBCO grains.<sup>20</sup> In contrast, the small-grain CeO-20 substrate supports high YBCO nucleation at much lower  $p(\text{O}_2)$  values, thus yielding films having  $J_c$  and  $H_{irr}$  of 4.2 MA/cm<sup>2</sup> and 4.5 T, respectively at 65 mTorr. The reported values of  $J_c$  at fields  $>1$  T and  $H_{irr}$  here, measured by the magnetization method are rather conservative, and in general lower than those obtained by the transport method due to high flux creep at 77 K.

XRD performed on the CeO-20 sample reveals a new structural transformation, closely correlated with the enhancement in the performance of this sample. Figure 1(b) shows the  $\theta$ - $2\theta$  XRD spectrum of the CeO-20 sample in the as-grown, tetragonal state (open symbols) and after 30 min oxygen annealing at 400 °C. Oxygen annealing induces formation of a new phase identified by two additional peaks, at

$2\theta \approx 5^\circ$  and  $10^\circ$ , superimposed on a set of (00 $l$ ) YBCO reflections. In the following we refer to this phase as A-type superstructure (SSa) and label the corresponding peaks SSa (002) and SSa (004). The preliminary reflection indexing is based on analogy of this diffraction pattern with that of the YBCO-Y248 mixed films.<sup>21</sup> The new phase appears only in samples processed at oxygen partial pressure below 100 mTorr, rapidly dissipating after high-temperature, high-oxygen partial pressure annealing. This observation confirms that the advantage of the substrate catalysis is most noticeable in the low  $p(\text{O}_2)$  region, in the proximity of YBCO stability line.<sup>22</sup> This is because, under the low  $p(\text{O}_2)$  growth conditions, the dominant phase, YBCO, becomes less stable, permitting the nucleation sites for the new phases.

The Pearson7 approximations, shown as solid lines, yield the superstructure peak positions at  $2\theta = 5.048(1)$  and  $10.050(5)$ , which correspond to the  $d$ -spacing values of  $1.748(1)$  and  $0.879(2)$  nm. From the positions of the YBCO (00 $l$ ) peaks, the  $c$ -axis parameter is  $1.168(1)$  nm, which is in agreement with the well known value of  $1.168\,04(1)$  nm for fully oxygenated YBCO. The closest reflection of a known YBCO derivative is (002) of Y248 at  $d = 1.36$  nm,<sup>23</sup> which makes the SSa structure distinctly different from the well-known derivative phases. The SSa peaks are noticeably broader than the YBCO matrix, suggesting that the SSa domains are small, on the order of 10 nm. Williamson–Hall analysis of the line profile shows that the YBCO matrix can be described as an agglomerate of very large ( $>1\,\mu\text{m}$  laterally and 350 nm in the  $c$  direction) domains with average microscopic out-of-plane tilt ( $\sim 0.6^\circ$ ) and relatively low rms strain ( $\sim 0.3\%$ ). The SSa domains appear to be much smaller,  $\sim 10$  nm in the  $c$  direction and 60 nm in the  $ab$  plane.

Thinner,  $0.1\,\mu\text{m}$  thick films deposited on CeO-20 allow for better identification of the phase composition due to lower film volume and large substrate contribution to the phase formation. As expected from the  $p(\text{O}_2)$ - $T$  diagram, growth at high  $p(\text{O}_2)$  level of 220 mTorr produces tetragonal YBCO phase [Fig. 2(a)], which after oxygen annealing transforms into the superconducting phase with  $T_c = 91$  K, as shown in Fig. 2(b). Reduction in  $p(\text{O}_2)$  to 160 mTorr results in the formation of a phase with  $c$ -axis parameter identical to that of Y248. The Y248 phase remains nonsuperconducting after the annealing procedure. It should be noted that the superconducting Y248 phase<sup>24</sup> ( $T_c = 81$  K) is stable at  $p(\text{O}_2) > 15$  Torr at  $780^\circ\text{C}$ ,<sup>25</sup> approximately two orders of magnitude higher  $p(\text{O}_2)$  level than the one employed for this study. Apparently, high level of structural disorder, evidenced by broadening of (00 $l$ ) peaks and the absence of high-order reflections, renders “low  $p(\text{O}_2)$ ” Y248 nonsuperconducting. Further reduction in  $p(\text{O}_2)$  down to 110 mTorr produces re-entrant YBCO phase, which has a diffraction signature almost identical to that of standard YBCO. The unique properties of the re-entrant YBCO become apparent after annealing at  $400^\circ\text{C}$  in oxygen [see Fig. 2(b)]. Approximately 90% of re-entrant YBCO transforms into the SSa phase and the sample becomes superconducting at 90 K. Thus,  $\theta$ - $2\theta$  spectra of the  $0.8\,\mu\text{m}$  film, Fig. 1(b), can be described as the transformation of intermixed re-entrant and

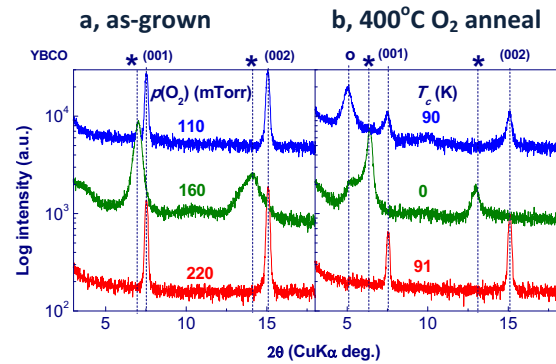


FIG. 2. (Color online) Phase formation in  $0.1\,\mu\text{m}$  CeO-20 films processed at various  $p(\text{O}_2)$  levels. Peaks of the SSa phase are labeled by “o” symbol and those corresponding to Y248 are labeled by “\*.” (a)  $\theta$ - $2\theta$  spectra of as-grown  $0.1\,\mu\text{m}$  CeO-20 samples, the numbers correspond to the  $p(\text{O}_2)$  level. After the  $p(\text{O}_2)$  level is reduced from 220 to 160 mTorr, a phase identified as Y248 completely displaces superconducting YBCO. Reduction in  $p(\text{O}_2)$  to 110 mTorr results in the formation of re-entrant YBCO, which appears to have a structural signature identical to that of standard YBCO. (b) Effect of 30 min annealing in oxygen at  $400^\circ\text{C}$ , the numbers correspond to  $T_c$ . Re-entrant YBCO transforms into the SSa phase, and subsequently the sample becomes superconducting at 90 K. Notably, the sample processed at 160 mTorr remains nonsuperconducting upon oxygen annealing.

standard YBCO phases. We conclude that it is the unique ability of CeO-20 substrates to nucleate re-entrant YBCO at very low  $p(\text{O}_2)$  values that is responsible for the phase transformations shown in Figs. 1(b) and 2.

## B. Stability of 3.5 nm derivative at elevated temperatures

The nonequilibrium nature of the SSa phase becomes apparent after annealing in oxygen at temperatures over  $500^\circ\text{C}$ . Figure 3(a) shows the evolution of the  $\theta$ - $2\theta$  spectra of  $0.8\,\mu\text{m}$  thick CeO-20 samples after 30 min oxygen annealing at  $550^\circ\text{C}$ ,  $600^\circ\text{C}$ , and  $700^\circ\text{C}$ , respectively. The solid lines are approximations of disordered layered crystal model by Hendricks *et al.*<sup>26</sup> that was adapted by Specht *et al.*<sup>5</sup> to measure the frequency of Y248 SF in YBCO films. The approximations show that initially the sample has low density of SFs,  $\text{SF} = 0.015$ , which is a typical value for Dy-doped YBCO.<sup>5</sup> The 248 SF density doubles after annealing at  $550^\circ\text{C}$ , at the same time both SSa (002) and SSa (004) peaks dissipate. A rise in the Y248 SF density at  $550^\circ\text{C}$  indicates that SSa starts to decompose into Y248. After the  $600^\circ\text{C}$  step, a new peak appears at  $2\theta = 12.3^\circ$  and multiple satellites form around the YBCO (003) peak. At  $700^\circ\text{C}$  the satellites transform into two distinct peaks. We interpret this transformation as the formation of another, shorter period, B-type superstructure (SSb), which is attributed to be a final decomposition product of SSa. The reflections correspond to  $d$ -spacing values of  $0.71(2)$  nm and  $0.35(1)$  nm, respectively. Stacking faults practically disappear upon annealing at  $700^\circ\text{C}$ , in agreement with the observation of Specht *et al.*<sup>5</sup>

The structural transformations shown in Fig. 3(a) correlate with the changes in the in-field  $J_c$ , plotted in Fig. 3(b). Transition from well-defined SSa peaks to a broad low-angle tail after annealing at  $550^\circ\text{C}$  changes the  $J_c(H)$  curve very little. However, after annealing at  $600^\circ\text{C}$   $J_c$  drops by a fac-



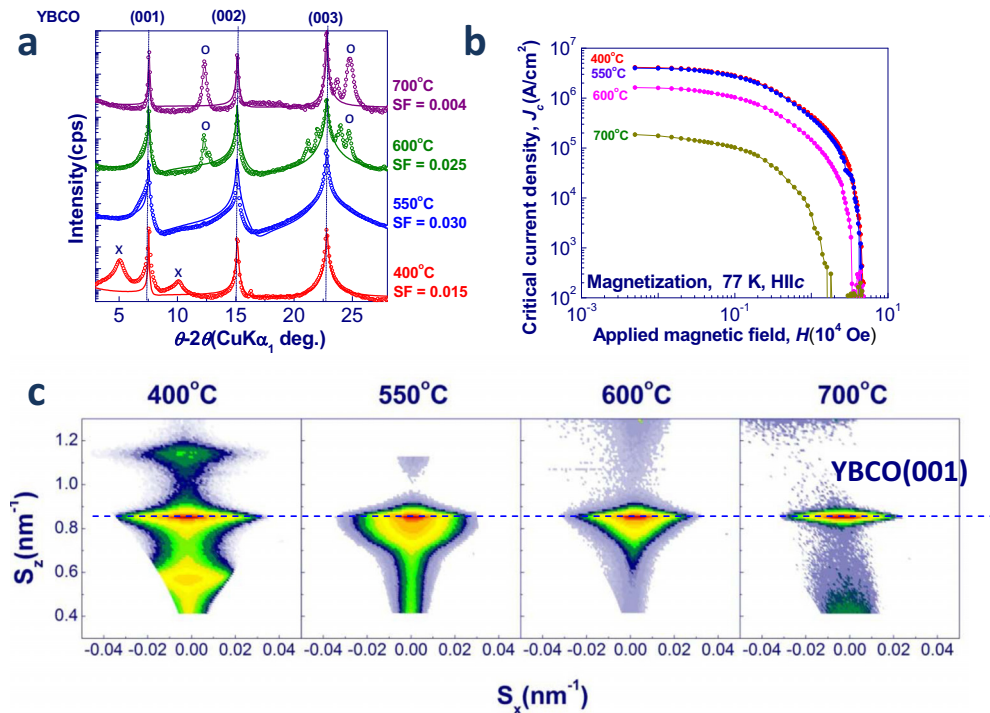


FIG. 3. (Color online) Effect of decomposition of the SSa phase after the high-temperature annealing of CeO-20 samples. (a) Evolution of  $\theta$ - $2\theta$  scans showing transformation of long-period SSa (reflections marked by “x” symbol) into shorter period SSb (reflections marked by “o” symbol) after annealing at  $>600$  °C. Note the development of multiple satellites around the YBCO (003) peak at 600 °C. One of the satellites transforms into a strong superstructure peak at 700 °C. Solid lines are approximations of the disordered crystal model (Refs. 5 and 26) used to determine the SF frequency presented on the right of each plot along with the annealing temperatures. (b) Change of the in-field critical current density of CeO-20 sample after high-temperature annealing. We relate the reduction in the performance to the relaxation of A-type superstructure and formation of B-type structure, (c) reciprocal space maps in the vicinity of the YBCO (001) reflection, showing collapse of the long-period superstructure after annealing at 600 °C. This event correlates with the threefold reduction in  $J_c$ , panel b). The horizontal line marks the position of the YBCO (001) reflection. The maps were recorded using 10 kV synchrotron radiation.

tor of three. Judging from the diffraction pattern spectrum, annealing at 550 °C completely destroys SSa domains with little effect on the  $J_c$ . An inspection of the reciprocal space maps in Fig. 3(c) reveals that even though domains lose long-range order in the  $c$ -direction, they still remain small laterally, as indicated by the broad diffuse feature below the YBCO (001) reflection. Decomposition of SSa domains at 600 °C results in the collapse of the broad feature below YBCO (001) peak, which also correlates with the reduction in the  $J_c$ . At the same time we observe development of a short-period SSb phase, a product of the decomposition of the SSa phase. The decomposition of the SSa and Y248 SFs is completed at 700 °C; after this annealing step  $J_c$  drops tenfold. Comparison of the line profiles of the (003) and (103) YBCO reflections before and after the 700 °C treatment shows that normal strain is not affected by the decomposition of the SSa phase, as indicated by the unchanged position and width of (003) reflection.

### C. Structure of 3.5 nm derivative

TEM analysis of the CeO-20 samples revealed multiple bright contrast regions embedded in the YBCO matrix. Figure 4(a) shows a TEM cross-section micrograph of one of the inclusions viewed along the [110] direction. The spacing of fringes along the [001] direction is 1.75 nm, identifying the inclusion as the SSa phase. Our structure model is based on an assumption that the SSa phase forms as a result of the re-arrangement of constituent ions, either anions (oxygen), or

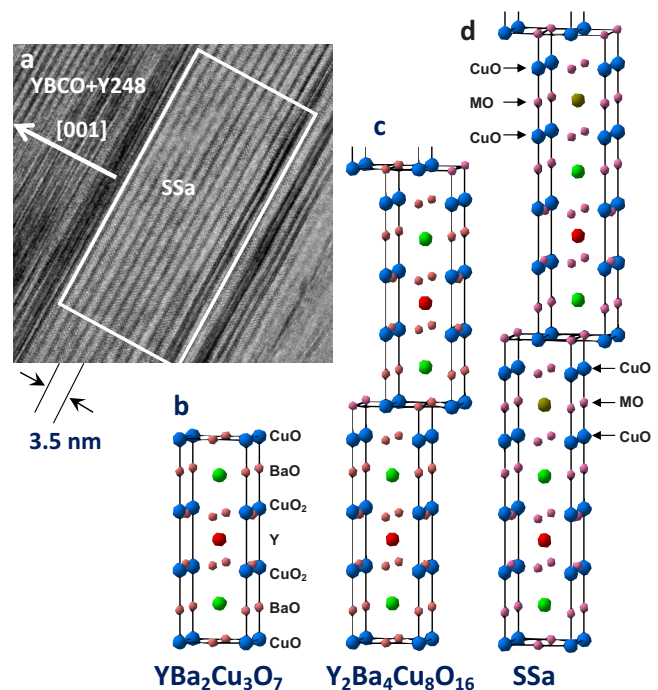


FIG. 4. (Color online) TEM analysis and structure model of SSa phase, (a) TEM cross-section of the SSa precipitate embedded in the YBCO+Y248 matrix viewed along the [110] direction. The white rectangle outlines the SSa inclusion. [(b)–(d)] Structure models of (b)  $\text{YBa}_2\text{Cu}_3\text{O}_7$ ,  $c=1.17$  nm, (c)  $\text{YBa}_2\text{Cu}_4\text{O}_8$ ,  $c=2.76$  nm, and (d) a model of SSa phase,  $c=3.5$  nm. The SSa model cell is formed by insertion of two  $\text{MO-CuO}$  ( $M=\text{Y}_{0.33}\text{Ba}_{0.67}$ ) double layers into a Y248 cell.

cations (yttrium, barium, copper) during the low-temperature oxygen anneal of re-entrant YBCO. The model based on simple oxygen ordering can be ruled out since the calculated XRD intensities of the superstructure reflections would be much lower than those observed due to the low scattering factor of oxygen. Since the SSa phase forms at a relatively low temperature (400 °C), the cation motion is limited to a short-range (<1 nm) diffusion. Thus the overall composition of the SSa phase should be close to that of YBCO or Y248. One possible cation arrangement can be realized by insertion of three extra layers of CuO, MO, and CuO, where *M* is the statistical mixture of Y and Ba with 33% Y and 67% Ba. Figures 4(b)–4(d) compares the structure models of the YBCO, Y248, and the SSa phases. In this model the SSa phase has an A-centered orthorhombic lattice with  $a=a_0$ ,  $b=b_0$ , and  $c=3c_0$ , where  $a_0$ ,  $b_0$ , and  $c_0$  are the lattice parameters of YBCO. The structure can also be presented as Y248 with extra MO/CuO double layers in each half cell. The extra double layers break the  $m_{x,y,0}$  mirror plane, thus reducing the symmetry to *Amm*2. The calculated XRD intensities based on this model match the experiments well. Currently, it is unclear what structural features of the re-entrant YBCO phase make the low-temperature formation of the SSa phase possible. The difference in the (00*l*) peak intensity ratio between re-entrant and regular YBCO  $\theta$ – $2\theta$  spectra is too small to attribute the transformation to an inter-layer cation disorder.<sup>27,28</sup>

## IV. DISCUSSION

We confirmed the presence of two metastable long-period YBCO derivatives. Both the derivatives can intercalate the YBCO matrix and provide extra magnetic flux pinning. One of them is the nonsuperconducting “low- $p(\text{O}_2)$ ” Y248 phase, which, when diluted in the YBCO matrix, exists as the well known Y248 SFs. The effect of SFs on  $J_c$  is well documented: several percent intercalation of YBCO films by Y248 results in a slightly higher  $J_c$  for  $H\parallel c$  and a much stronger  $J_c$  enhancement for  $H\parallel ab$  orientations.<sup>5,29</sup> The insulating nature of “low- $p(\text{O}_2)$ ” Y248 limits the maximum allowable content of this phase in the YBCO matrix. Using the active substrates, like CeO-20, we can easily change the SF content, however samples with the SF frequency >0.1 are nonsuperconducting. In contrast, the other YBCO derivative, the previously unknown long-period SSa phase, has a remarkable effect on  $J_c$  and  $H_{irr}$ . The unique features of the SSa phase include strong pinning at the  $H\parallel c$  orientation along with apparent absence of  $T_c$  degradation even at a very high volume fraction. We rule out direct flux pinning by SSa domains because, according to TEM and diffraction data, the domains are platelike inclusions extending over 50 nm in the *ab* plane. In comparison, effective artificial pinning centers, such as oxide nanorods,<sup>8,30–32</sup> extend in the *ab* plane by less than 10 nm. A more likely possibility is that the YBCO-SSa transformation builds internal stress in the film. The stress does not relax due to the very low temperature, 400 °C, of the transformation. Indeed, high rms strain generated by nanoinclusions is thought to be the source of the record pinning force in thin YBCO films.<sup>33</sup> Profile analysis of the

YBCO (00*l*) reflections did not reveal a meaningful change in the normal rms strain that might be associated with formation and decomposition of the SSa phase. This is not unexpected given that the SSa phase is commensurate with the YBCO matrix in the *c*-direction,  $c(\text{SSa})=3\times c(\text{YBCO})$ . Presence of the lateral rms, which would imply lateral deformation of the YBCO matrix by the SSa phase, is yet to be confirmed by the high-resolution in-plane x-ray scattering.

## V. CONCLUSION

In conclusion, we demonstrated a new promising direction for materials exploration using strong solid state catalysis. Here a relatively simple arrangement of a planar active substrate was utilized to catalyze the formation of new phases. More complex configurations, for example, three-dimensional arrays of oriented catalytically active nanorods can be utilized in the future to provide greater process flexibility and make the synthesis more scalable. It is yet to be determined whether the new metastable phases, SSa, is a superconductor and if so, whether its properties are superior to those of YBCO. In our view, the most important question is whether the SSa phase alone or SSa-YBCO composites are more tolerant to the grain boundary misalignment compared to regular YBCO.

## ACKNOWLEDGMENTS

We are grateful to American Superconductor Corporation (M. Rupich and X. Li) for providing precursor films used in this study. We acknowledge the technical support of the Center for Functional Nanomaterials and National Synchrotron Light Source (Beamline X-18A), at Brookhaven National Laboratory. Particularly, we'd like to thank Steven Ehrlich for the assistance during the X-18A beamline experiments, Eliot Specht for providing the source code used in the x-ray data analysis and Ivo Dimitrov for suggestions. The work at Brookhaven National Laboratory was supported by the U.S. Department of Energy under Contract No. DEAC02-98CH10886 with the Office of Electricity Delivery and Energy Reliability (Solovyov) and the Office of Basic Energy Science (Si, Wu, Zhou, Qing, and Li).

<sup>1</sup>A. Saxena and G. Aeppli, MRS Bull. **34**, 804 (2009).

<sup>2</sup>Z. Islam, S. K. Sinha, D. Haskel, J. C. Lang, G. Srajer, B. W. Veal, D. R. Haefner, and H. A. Mook, Phys. Rev. B **66**, 092501 (2002).

<sup>3</sup>R. M. Fleming, L. F. Schneemeyer, P. K. Gallagher, B. Batlogg, L. W. Rupp, and J. V. Waszczak, Phys. Rev. B **37**, 7920 (1988).

<sup>4</sup>H. W. Zandbergen, R. Gronsky, K. Wang, and G. Thomas, Nature (London) **331**, 596 (1988).

<sup>5</sup>E. D. Specht, A. Goyal, J. Li, P. M. Martin, X. Li, and M. W. Rupich, Appl. Phys. Lett. **89**, 162510 (2006).

<sup>6</sup>V. Selvamanickam, Y. Chen, X. Xiong, Y. Y. Xie, J. L. Reeves, X. Zhang, Y. Qiao, K. R. Lenth, R. M. Schmidt, A. Rar, D. W. Hazelton, and K. Tekletsadik, IEEE Trans. Appl. Supercond. **17**, 3231 (2007).

<sup>7</sup>A. Malozemoff, Adv. Mater. Proc. **165**, 35 (2007).

<sup>8</sup>B. Maiorov, S. A. Baily, H. Zhou, O. Ugurlu, J. A. Kennison, P. C. Dowden, T. G. Holesinger, S. R. Foltyn, and L. Civale, Nature Mater. **8**, 398 (2009).

<sup>9</sup>T. G. Holesinger, L. Civale, B. Maiorov, D. M. Feldmann, J. Y. Coulter, J. Miller, V. A. Maroni, Z. J. Chen, D. C. Larbalestier, R. Feenstra, X. P. Li, M. B. Huang, T. Kodanandath, W. Zhang, M. W. Rupich, and A. P. Malozemoff, Adv. Mater. **20**, 391 (2008).

<sup>10</sup>T. Aytug, M. Paranthaman, E. D. Specht, Y. Zhang, K. Kim, Y. L. Zuev, C. Cantoni, A. Goyal, D. K. Christen, V. A. Maroni, Y. Chen, and V. Selva-

- manickam, *Supercond. Sci. Technol.* **23**, 014005 (2010).
- <sup>11</sup>H. Zhou, B. Maiorov, S. A. Baily, P. C. Dowden, J. A. Kennison, L. Stan, T. G. Holesinger, Q. X. Jia, S. R. Foltyn, and L. Civale, *Supercond. Sci. Technol.* **22**, 085013 (2009).
  - <sup>12</sup>A. Trovarelli, C. de Leitenburg, M. Boaro, and G. Dolcetti, *Catal. Today* **50**, 353 (1999).
  - <sup>13</sup>X. Obradors, T. Puig, A. Pomar, F. Sandiumenge, N. Mestres, M. Coll, A. Cavallaro, N. Romà, J. Gázquez, J. C. González, O. Castaño, J. Gutierrez, A. Palau, K. Zalamova, S. Morlens, A. Hassini, M. Gibert, S. Ricart, J. M. Moretó, S. Piñol, D. Isfort, and J. Bock, *Supercond. Sci. Technol.* **19**, S13 (2006).
  - <sup>14</sup>V. F. Solovyov, K. Develos-Bagarinao, Q. Li, J. Qing, and J. Zhou, *Supercond. Sci. Technol.* **23**, 014008 (2010).
  - <sup>15</sup>V. F. Solovyov, K. Develos-Bagarinao, and D. Nykypanchuk, *Phys. Rev. B* **80**, 104102 (2009).
  - <sup>16</sup>D. M. Feldmann, T. G. Holesinger, R. Feenstra, and D. C. Larbalestier, *J. Am. Ceram. Soc.* **91**, 1869 (2008).
  - <sup>17</sup>D. Dimos, P. Chaudhari, J. Mannhart, and F. K. LeGoues, *Phys. Rev. Lett.* **61**, 219 (1988).
  - <sup>18</sup>A. P. Malozemoff, S. Fleshler, M. Rupich, C. Thieme, X. Li, W. Zhang, A. Otto, J. Maguire, D. Foltz, J. Yuan, H. P. Kraemer, W. Schmidt, M. Wohlfart, and H. W. Neumueller, *Supercond. Sci. Technol.* **21**, 034005 (2008).
  - <sup>19</sup>P. C. McIntyre, M. J. Cima, J. A. Smith, R. B. Hallock, M. P. Siegal, and J. M. Phillips, *J. Appl. Phys.* **71**, 1868 (1992).
  - <sup>20</sup>V. F. Solovyov, Q. Li, H. Wiesmann, P. Oleynikov, and Y. Zhu, *Supercond. Sci. Technol.* **21**, 125013 (2008).
  - <sup>21</sup>K. Char, M. Lee, R. W. Barton, A. F. Marshall, I. Bozovic, R. H. Hammond, M. R. Beasley, T. H. Geballe, A. Kapitulnik, and S. S. Laderman, *Phys. Rev. B* **38**, 834 (1988).
  - <sup>22</sup>J. L. MacManus-Driscoll, *Adv. Mater.* **9**, 457 (1997).
  - <sup>23</sup>P. Marsh, R. M. Fleming, M. L. Mandich, A. M. DeSantolo, J. Kwo, M. Hong, and L. J. Martinez-Miranda, *Nature (London)* **334**, 141 (1988).
  - <sup>24</sup>J. Karpinski, E. Kaldis, E. Jilek, S. Rusiecki, and B. Bucher, *Nature (London)* **336**, 660 (1988).
  - <sup>25</sup>D. E. Morris, A. G. Markelz, B. Fayn, and J. H. Nickel, *Physica C* **168**, 153 (1990).
  - <sup>26</sup>S. Hendricks and E. Teller, *J. Chem. Phys.* **10**, 147 (1942).
  - <sup>27</sup>G. Gibson, L. F. Cohen, R. G. Humphreys, and J. L. MacManus-Driscoll, *Physica C* **333**, 139 (2000).
  - <sup>28</sup>J. A. Agostinelli, S. Chen, and G. Braunstein, *Phys. Rev. B* **43**, 11396 (1991).
  - <sup>29</sup>J. Gutiérrez, B. Maiorov, T. Puig, J. Gázquez, N. Romà, H. Wang, F. Sandiumenge, and X. Obradors, *Supercond. Sci. Technol.* **22**, 015022 (2009).
  - <sup>30</sup>S. A. Harrington, J. H. Durrell, B. Maiorov, H. Wang, S. C. Wimbush, A. Kursumovic, J. H. Lee, and J. L. MacManus-Driscoll, *Supercond. Sci. Technol.* **22**, 022001 (2009).
  - <sup>31</sup>S. H. Wee, A. Goyal, J. Li, Y. L. Zuev, and S. Cook, *J. Appl. Phys.* **102**, 063906 (2007).
  - <sup>32</sup>J. L. MacManus-Driscoll, S. R. Foltyn, Q. X. Jia, H. Wang, A. Serquis, L. Civale, B. Maiorov, M. E. Hawley, M. P. Maley, and D. E. Peterson, *Nature Mater.* **3**, 439 (2004).
  - <sup>33</sup>J. Gutiérrez, A. Llordes, J. Gázquez, M. Gibert, N. Romà, S. Ricart, A. Pomar, F. Sandiumenge, N. Mestres, T. Puig, and X. Obradors, *Nature Mater.* **6**, 367 (2007).